Convective dissolution of carbon dioxide into brine in a three-dimensional free medium

Paul Fruton, Aziza Nauruzbaeva, Henri Bataller, and Cédric Giraudet
Universite de Pau et des Pays de l'Adour, E2S UPPA, CNRS, TotalEnergies, LFCR UMR5150, Anglet, France

Alberto Vailati
Dipartimento di Fisica Aldo Pontremoli, Università degli Studi di Milano, Milano, Italy

Fabrizio Croccolo*
Universite de Pau et des Pays de l'Adour, E2S UPPA, CNRS, TotalEnergies, LFCR UMR5150, Anglet, France

(Received 7 May 2022; accepted 6 February 2023; published 27 February 2023)

When carbon dioxide (CO_2) is layered on top of brine, the diffusion occurring at the interface generates an intermediate layer denser than the brine one. This may generate a convective process that accelerates CO_2 dissolution into the brine. Here, we use the shadowgraph method and a sample cell geometry with a large width/height aspect ratio to investigate the 3D behavior of the convective dissolution of CO_2 in brine in a free medium. This process is driven by the instability of the denser boundary layer formed at the interface between the two phases and is totally independent of the overall vertical size. When the purely diffusive mass transfer get disrupted, we observe the development of complex 3D structures, consisting of CO_2-rich falling sheets at the liquid-liquid interface. This pattern could not be detected in 2D Hele-Shaw studies, mainly used in the literature. The experiments have been performed over a broad range of CO_2 pressures, close to the process-relevant conditions, and show that the convective mass transfer is governed by the critical thickness of the mixing layer at the onset of convection, and that the process can be described by a scale-free universal model.

DOI: 10.1103/PhysRevFluids.8.023503

I. INTRODUCTION

Carbon capture utilization and storage (CCUS) can be a valuable support technology to achieve the net zero-emission target necessary to mitigate the impact of carbon dioxide (CO_2) on climate change [1–3]. The storage of CO_2 in underground reservoirs represents an indispensable step of CCUS. A huge amount of CO_2 can be stored in saline aquifers where the CO_2 is sequestered by dissolution. This process is strongly accelerated by the convective dissolution of CO_2 in brine [4–7] that highly enhances the dissolution rate.

Nowadays, the convective dissolution process has been well characterized for two-dimensional geometries, low permeabilities, and small injection-pressures of CO_2 [8,9]. The investigations focus on the impact of brine composition [4,5,10,11] and porous medium permeability [12–14] on the onset time of convection. These studies were conducted in a Hele-Shaw geometry [5,15–22], a configuration where mass transfer takes place in the Rayleigh-Darcy regime, suitable to model the process in a porous medium [23].

*fabrizio.croccolo@univ-pau.fr

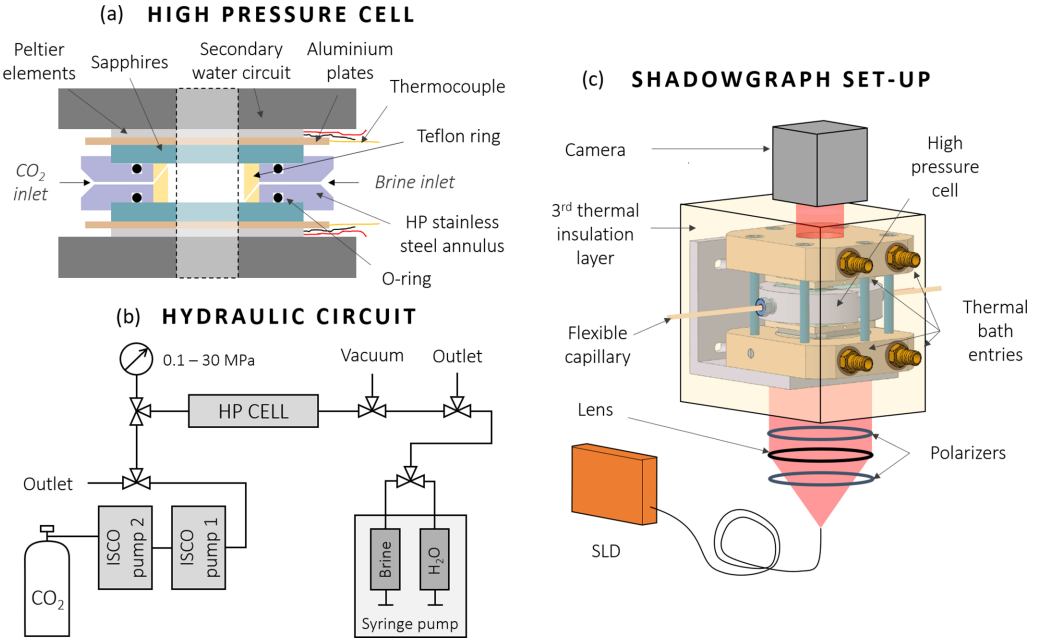

FIG. 1. Schematic of (a) the high-pressure cell, (b) the hydraulic circuit, and (c) the shadowgraph.

The model system employed to investigate the convective dissolution is represented either by a layer of brine overlaid with CO_2 at a controlled pressure or equivalent fluids, i.e., fluids exhibiting an inversion of the density profile upon mixing. Indeed, while CO_2 dissolves into brine, an interfacial liquid layer with a density larger than that of the underlying brine grows diffusively in the bulk [24]. When the density difference and the layer thickness are sufficiently large, a solutal convective instability takes place in the form of plumes [8]. The stability of the fluid against convection is determined by the balance between the driving force of buoyancy and the dissipating effects of viscosity and mass diffusion, as expressed by the dimensionless solutal Rayleigh number

$$\mathrm{Ra_s} = \frac{g\Delta\rho h^3}{\eta D}, \tag{1}$$

where g is the gravity acceleration, $\Delta\rho$ is the density difference between the interfacial liquid layer and the bulk, η and D are the dynamic viscosity and the Fick diffusion coefficient at macroscopic thermodynamic equilibrium, and h the liquid layer thickness.

Here, we observe the system made of gaseous CO_2 and liquid brine layered in the direction parallel to gravity in a three-dimensional (3D) cylindrical cell with a large width-to-height ratio. Our study highlights that the convective instability has a complex 3D structure with interconnected interfacial patterns that are not observable with the transversal observation of a Hele-Shaw cell. We provide experimental evidence that the onset time of convection and the dissolution rate are entirely dominated by the critical thickness of the boundary layer. Similar findings were observed for Rayleigh-Bénard thermal convection in a single component fluid [25–28].

II. EXPERIMENTAL METHODS

We performed experiments in a 5-mm-thick and 20-mm-large cylindrical high-pressure cell, see Fig. 1(a). It consists of a polytetrafluoroethylene (PTFE) ring inserted inside a stainless-steel block that is vertically confined between two sapphire windows. Since PTFE is highly hydrophobic, a thin layer of a hydrophilic polymer was added to the PTFE ring interior to have an almost flat gas-liquid interface. The cell hosts one inlet close to the upper window to inject the gas and one inlet close

to the bottom window to inject the brine, as visible in Fig. 1(a). It is thermally controlled with two Peltier elements, a thermal bath, and three insulation layers to work at a constant temperature of 308.2±0.5 K. The injection of CO_2 is performed by two ISCO DM500 pumps that keep the pressure constant during the time of the experiment; see Fig. 1(b).

The cell can be positioned in two different configurations: either in a horizontal one where the cylinder axis is perpendicular to gravity providing a transverse observation or observing from above in a vertical configuration where the cylinder axis is parallel to gravity. In any configuration, the inclination of the horizontal side of the cell is monitored with a calibrated inclinometer from Digi-Pas (DWL5000XY) and tuned to better than 9 mrad.

The optical technique used is that of a shadowgraph [29–32] comprising a super-luminous diode from Superlum with a wavelength of 675 ± 13 nm, coupled to a single mode optical fiber as a light source; see Fig. 1(c). The diverging beam out of the fiber is collimated by using an achromatic doublet lens of focal length 250 mm positioned at the focal distance from the lens. Two polarizers complete the illumination section to finely tune the intensity of the light impinging on the sample cell and optimize the optical contrast on the recorded images. A scientific complementary metal-oxide-semiconductor (s-CMOS) camera (Hamamatsu, ORCA-Flash4.0 V3) with a resolution of 2048×2048 pixels of 6 μm is placed at a distance of about 100 mm from the sample plane. During any experimental run, images are acquired at 20 or 2 Hz according to the experiment dynamics. The complete setup is mounted on a vibration-damped optical table. A drawing of the optical arrangement can be found in Ref. [33].

At the beginning of an experiment, the cell is first evacuated and then filled at atmospheric pressure with CO_2 from Linde with a purity better than 99.995 vol%. This limits the influence of residual gases contained in the atmosphere on dissolution. Then, a (2 ± 0.5)-mm-thick liquid layer, presaturated with CO_2 at atmospheric pressure, is injected from the bottom inlet using a syringe pump with a flow rate of 1 mL min^{-1}. The liquid volume is calibrated previously by performing experiments in the horizontal configuration, where the precise level of the liquid layer can be measured. The liquid consists of distilled water of Millipore grade and sodium chloride (NaCl) purchased from Fischer-Scientific. Both were degassed separately with the help of a two-stage oil-sealed rotary vane vacuum pump for about 30 min. The purity by mass of NaCl specified by the supplier is 99.5%. All brine mixtures were prepared gravimetrically with the help of a balance from Ohaus (Scout^{TM}) with a specified precision of 1 mg, where an absolute expanded measurement uncertainty of 0.2% was estimated. Three brine concentrations of 0, 1, and 3 mol kg^{-1} are used in this paper.

After the injection of CO_2 presaturated brine, the vapor-liquid equilibrium is reached at a temperature of 308.2±0.5 K, and CO_2 pressure is rapidly increased. The temperature has been chosen to remain far from the upper critical end point of the system CO_2-brine and avoid critical effects. The pressure difference applied to the system ranges from 0.34 to 6 MPa. The injection lasts 5 to 12 seconds and cannot be faster to prevent strong deformation of the interface and splashes on the upper sapphire that would make it impossible to analyze the images. Further experiments were conducted at pressure differences up to 10 MPa, where the injected CO_2 is in supercritical state. However, for pressure differences larger than 6 MPa, the injection induces turbulent flows in the CO_2 layer hindering the observation of convection in the liquid phase. Nevertheless, since the amount of CO_2 dissolved in brine does not vary much between 6 and 30 MPa at a temperature of 308.2 K [34] and that the systems are always biphasic for temperatures larger than about 304.5 K, the present results are directly transferable to process engineering conditions.

Shortly after the pressure increase, the formation and dissipation of convective patterns are visualized by the shadowgraph optical technique, routinely employed in our laboratories for investigating nonequilibrium fluctuations [29] and convective instabilities [32]. During the dissolution process, shadowgraph images are continuously grabbed until macroscopic thermodynamic equilibrium is reached. We mainly investigated the growth and relaxation of patterns in the vertical configuration of the setup while other experiments have been performed in the horizontal configuration close to the Hele-Shaw geometry with a large width to height ratio.

III. RESULTS

The initial pressure increase determines a transient diffusion process that eventually leads to convection. The left part of Fig. 2 shows typical shadowgraph images acquired after the pressure is increased from 0.1 to 2.1 MPa for CO_2 layered on top of water. The corresponding movie can be found in the Supplemental Material [35]. The side of the images included in Figs. 2(a)–2(h) is of 10.1 mm, smaller than the sensor size due to a slight lensing effect induced by the bending of the meniscus after CO_2 injection, as clearly visible at the early stage of the movie. The image processing consists of normalizing each image by its average intensity value and then subtracting them by a reference image. The reference image, or background, corresponds to the average intensity map between five normalized images acquired before the injection of CO_2. Then, the image difference is filtered in the Fourier space retaining only wave vectors in the range 43 to 350 cm^{-1}. Thereafter, we apply an inverse Fourier transform and compute the variance $\langle \delta i^2 \rangle$ of each filtered image difference, where the averaging is performed on all the pixels of each image difference. The variance provides a quantitative estimation of the mean squared amplitude of the variations of the refractive index determined by the formation of convective structures, as shown in the right part of Fig. 2. The image variance is a simple and reliable integrated information about the development of convective instabilities [32]. Here, the vertical position of the convective patterns is not affecting the variance. In fact, at small wave vectors, the Shadowgraph sensitivity varies less than 2% within the liquid layer. In some images, caustics appear, showing the nonlinearity of the Shadowgraph, so the variations of image intensity cannot be directly related to refractive index ones. The focus of this paper being more on the system dynamics, the resulting information remains however fully quantitative.

The time evolution of the image difference variance allows us to identify eight different phases denoted by Figs. 2(a)–2(h). They can be grouped in two main categories: the growth (A) and relaxation (B) of patterns.

A. Growth of convective patterns

After a short initial phase where the injection of CO_2 determines transient disturbances in the vapor phase, Fig. 2(a), the contrast of image differences remains constant, Fig. 2(b). This featureless stage corresponds to the diffusive growth of a CO_2-rich liquid boundary layer formed at the vapor-liquid interface [36] and ends at the onset time of convection t_c, when the thickness of the boundary layer is sufficiently large to trigger buoyancy-driven instabilities. This determines a sharp increase in the contrast and the appearance of patterns, Fig. 2(c). In conventional experiments observing the sample from the side, e.g., in Hele-Shaw cells, the onset time of convection is defined when the first plume detaches from the liquid-liquid interface. That is difficult to evaluate due to the presence of the meniscus inducing an overestimation of t_c. In our paper, the observation from above prevents from meniscus issues thus allowing a precise estimation of the onset time of convection. In fact, in Fig. 2(c), we observe a modification of the boundary layer, while plumes have not yet formed.

Then, these convective patterns are first characterized by the presence of falling sheets at the liquid-liquid interface. Gradually, additional falling sheets appear and break to feed discrete falling plumes, propagating vertically into the bulk, Figs. 2(d) and 2(e), until the optical contrast reaches its maximum, Fig. 2(e), at time t_m. The convective pattern is complete and has spread all over the liquid-liquid interface while the mixing inside the bulk has just started. Thus, the density difference between the highly concentrated sheets and the bulk, $\Delta\rho$, has not decreased yet and the dissolution rate is maximum at t_m.

B. Relaxation of convective patterns

The pattern's rapid growth is followed by relaxation processes. A first relaxation determines a decrease of the contrast in a time t_r to an almost constant value, corresponding to a stable regime where the convective flux can be assumed constant. Here, the flow of CO_2 takes place mostly through steady plumes taking the form of columns crossing the bulk from the liquid-liquid interface

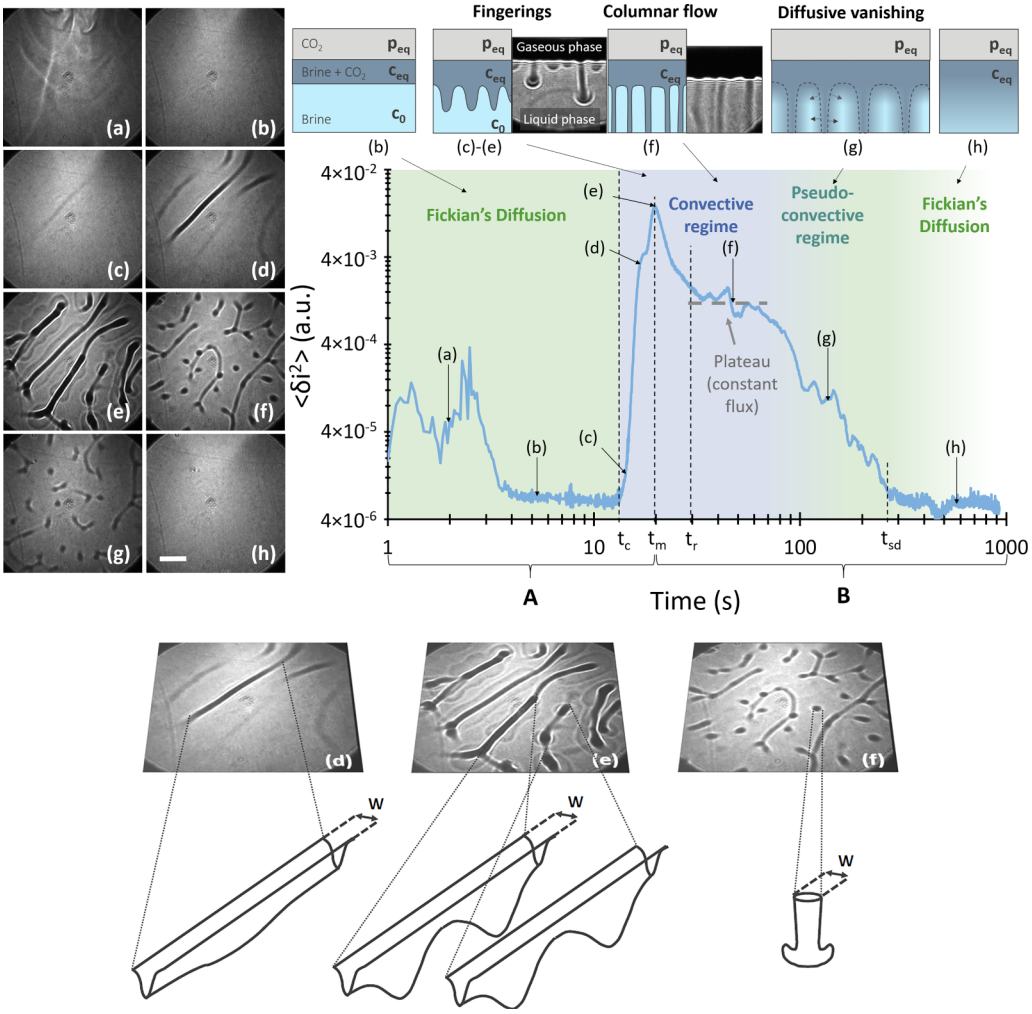

FIG. 2. 3D spatiotemporal evolution of the convective dissolution process for CO_2 dissolved in pure water for a pressure increase from 0.1 to 2.1 MPa. Top-left panel: Shadowgraph images taken at different times of the process. Top-right panel: Time evolution of the variance $\langle \delta i^2 \rangle$ of shadowgraph image differences. The top inserts show schematically the boundary layer and the patterns with representative images obtained from transversal observation. (a) The injection temporarily perturbs the contrast until the gaseous phase becomes stable and the contrast constant. (b) During this regime, CO_2 spreads diffusively into water, giving rise to an unstable growing boundary layer. (c) At $t = t_c$, the contrast rises and convective patterns suddenly appear. (d) After a short time, the first pattern reaches the maximum concentration C_{eq} of CO_2 and further patterns appear. (e) The image variance reaches a maximum at t_m. (f) The plateau characterizes a stationary condition where the boundary layer thickness and the convective flux are constant. Here, the convective flow is essentially made of plumes. (g) The convective flow gradually mixes CO_2 and water in the entire bulk, and patterns become less and less contrasted as they are dissipating diffusively. (h) Convection vanishes and the variance goes back to its initial level. The size bar in (h) corresponds to the water layer thickness h=2 mm. Bottom panel: Schematic representation of the convective patterns. Left: Falling sheet at the early stage; middle: falling sheets breaking into plumes after accumulating dissolved CO_2; right: isolated plume at late stage of convection.

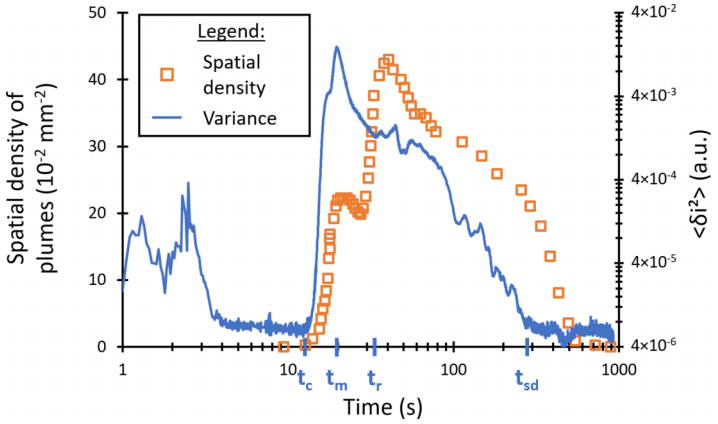

FIG. 3. Plume density measured from the shadowgraph images for an injection from 0.1 to 2.1 MPa (orange square symbols) plotted against optical contrast as in Fig. 2 (blue continuous line). After t_c, plumes appear within the sheets and the plume density rises. The latter reaches a first maximum around t_m, decreases and rapidly increases again after t_r due to the appearance of isolated plumes. Then, the plume density decreases and vanishes after t_{sd} that corresponds to the end of the convective regime. The typical timescales defined in Fig. 2 have been reproduced here on the axis of time.

to the cell bottom, Fig. 2(f). The origin of the variance decrease is twofold. First, the initial falling sheets start to collapse in plumes. Even though there are still signatures of the sheets still remaining and new isolated plumes emerging, this process leads to the creation of pattern-free areas at a larger proportion than at t_m. Second, after t_m, $\Delta\rho$ starts to decrease as plumes are reaching the bottom of the cell, which explains the reduced contrast, Fig. 2(f), between the bulk and the patterns with respect to t_m.

As the height of the liquid layer h is relatively small in our setup, the mixing inside the entire bulk starts immediately after the plumes touch the bottom of the cell. Then, the density difference between the boundary layer and the surrounding CO_2-poor layer is rapidly decreasing, inducing, after the constant flux regime, a second relaxation taking place until the shutdown of the convective regime at t_{sd}. Convection cannot be sustained any more since the CO_2 dissolved into the fluid has almost reached its saturation concentration in the bulk, Fig. 2(g), meaning that $\Delta\rho$ is too small. Here, the remaining patterns are dissipating diffusively in the bulk and, after some time, the contrast reaches its initial value, Fig. 2(h), where the system is at macroscopic thermodynamic equilibrium. As reflected by the small jumps in the contrast, the relaxation process exhibits intermittency, determined by the random emergence of new plumes. The 3D spatiotemporal evolution of growth and dissipation of convective patterns was found qualitatively similar for both water and brine, independently of the salt concentration and the pressures of injection.

C. Spatial scales

From the analysis of the shadowgraph images, we additionally obtain the time evolution of the plume density, defined as the number of plumes per surface area. The measurement of the spatial density of plumes has been made by determining the number of nodes corresponding to a downward plume on each image. The comparison between the plume density and the image contrast (Fig. 3) provides a further insight in the convective dissolution process. While the variance of image differences shows one maximum, the plume density presents two peaks. The first one takes place at the end of the phase of growth of convective patterns t_m. Advection is led by the maximum formation of plumes which are mostly located at the sheet crest. Immediately after, isolated plumes and sheets merge, resulting in a small decrease of their density. The second peak occurs when the

image difference contrast reaches a plateau. In the first phase of relaxation, the formation of new plumes comes at the expense of the breaking of falling sheets, as witnessed by the decrease in the variance. While some sheet patterns remain at this moment [Fig. 2(f)], the plume/column density is at its maximum and the variance is almost constant. Finally, the plumes density decreases until it reaches zero after t_{sd}. Indeed, when the image contrast has reached its baseline value, there are still some patterns in the bulk that get very small contrast. The shutdown of convection actually takes place at t_{sd}, after which the remaining columns fade away by diffusion only. From the analysis of similar curves for different injection pressures, we note that the maximum plume density increases with the Rayleigh number.

We also measure the width w of the plumes, as shown in the bottom part of Fig. 2. Due to the poor contrast of the patterns, their width is estimated with a large error. Thus, according to the measurement uncertainties, the width seems to be constant during the experiment. Nevertheless, we observe a clear tendency: the higher the Rayleigh number, the larger the convective patterns.

IV. DISCUSSION

A quantitative understanding of the scaling relation for the onset time, and in turn of the physical mechanism behind the instability, can be achieved by considering the seminal model developed by Howard to describe the onset of turbulent Rayleigh-Bénard convection in a horizontal layer of a single component fluid of infinite aspect ratio subjected to a temperature difference well above the threshold for convection [37]. Under these conditions, heat conduction determines the rapid growth of a temperature boundary layer, which becomes unstable when it reaches a critical thickness. The instability determines the emission of plumes, which deplete the boundary layers, and the process iterates until the system reaches a stationary state where the boundary layer thickness is pinned at its critical value. Arguments similar to those proposed by Howard have been successfully used to understand the onset of solutal boundary layer convection in suspensions of silica particles [38–40] and thermosensitive particles [41,42] triggered by the Soret effect, and during the dissolution of a solid into a liquid phase [43,44].

In our experiments, the imposition of a sudden jump of the pressure of CO_2 at the beginning of the experiment determines an increase of the CO_2 solubility. Thus, CO_2 gradually diffuses into the liquid phase and forms a mixed liquid boundary layer at the two-phase interface. Since the density of mixtures of CO_2 and water (brine) is larger than that of water (brine) itself, the boundary layer is intrinsically unstable against gravity [24]. Before convection sets in, the time evolution of the diffusive growth of the boundary layer can be described analytically by solving the diffusion equation $\partial c/\partial t = D(\partial c/\partial z)^2$. The CO_2 phase can be modeled by adopting a boundary condition of constant concentration of CO_2 dissolved into water (brine) at the interface, while for the bottom water (brine) layer, one can assume impermeable boundary conditions. For times much shorter than the diffusive time of the liquid layer $t_D = h^2/(\pi D)$ or for large sample thickness h, the concentration profile can be approximated by the one obtained in a semi-infinite system, with the top boundary at concentration C_{eq} and the bulk of the fluid at C_0, yielding $C(z) = C_0 + (C_{eq} - C_0)erfc[(h - z)/(\sqrt{4Dt})]$ [45]. Here, z is the vertical coordinate, $z = 0$ represents the bottom of the sample, and the interface is located at $z = h$.

The systematic investigation of the injection of CO_2 at different pressure steps shows that the dimensionless onset time $\tau_c = t_c/t_D$ exhibits a power-law behavior as a function of the solutal Rayleigh number Ra_s, with exponent $-(0.64 \pm 0.05)$, see Fig. 4(a). Here, the Rayleigh numbers have been computed using the procedure given in Appendix, and its values can be found in Table I. Interestingly, the time needed for the onset of convection is down to two orders of magnitude smaller than the diffusive time t_D needed to diffuse over the entire liquid layer, even if the latter is as thin as 2 mm, i.e., very thin compared to storage reservoirs that can achieve several hundreds of meters.

To model the onset of convection, we assume that the concentration profile in the liquid layer can be divided into two regions: a boundary layer region at the top, where the concentration varies as an error function from the initial to the equilibrium value, and a bulk region at the bottom, where

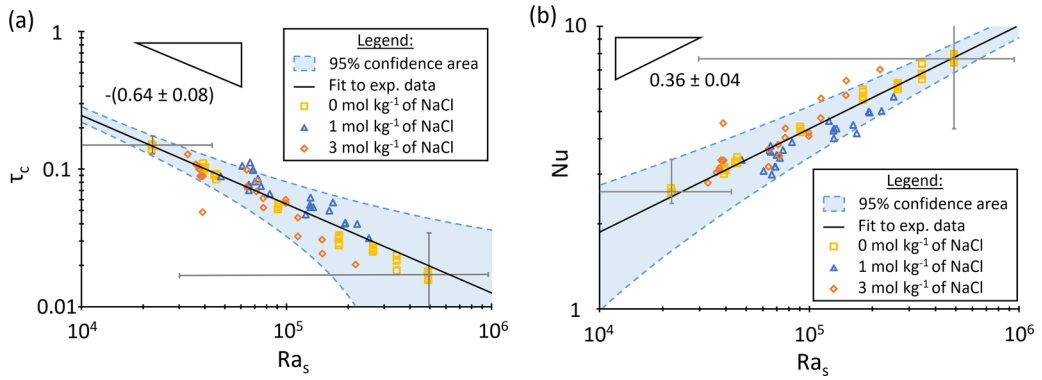

FIG. 4. Log-log plots of (a) the dimensionless onset time $\tau_c = t_c/t_D$ as a function of the solutal Rayleigh number and (b) Solutal Nusselt number $Nu_s = h/d^* = h/\sqrt{\pi D t_c}$ as a function of the solutal Rayleigh number. Experimental data are plotted with yellow squares (pure water), blue triangles (brine at 1 mol kg^{-1} of NaCl), and orange diamonds (brine at 3 mol kg^{-1} of NaCl). The continuous black line corresponds to the fit to experimental data with a power law: $\tau_c = 91\,Ra_s^{-0.64}$. The blue shaded area corresponds to the 95% confidence level of the fit to the experimental data. Error bars illustrate the expanded uncertainties ($k = 2$) of experimental data. Large error bars in Ra_s are mainly associated with the large experimental uncertainty of the liquid layer thickness. The expanded experimental uncertainties of τ_c and Ra_s have been derived using the uncertainties on t_c and h as well as the uncertainties on the other thermophysical properties taken from the literature. The standard deviation between repeated measurements is much smaller than the corresponding experimental uncertainty.

the concentration is essentially uniform. Following Howard, the thickness d of the boundary layer, estimated as the vertical extension of the linear region, changes in time diffusively as $d(t) = \sqrt{\pi D t}$, and in dimensionless form [37]

$$\delta(\tau) = d/h = \sqrt{\tau}. \tag{2}$$

During the initial diffusive growth, the boundary layer is horizontally uniform (except for tiny nonequilibrium concentration fluctuations [46]) and the contrast of shadowgraph images does not change significantly. When the boundary layer reaches the critical thickness δ^*, it becomes unstable and convection sets in at time τ^*; thereafter, plumes start to cross the cell in the vertical direction. The stability of the boundary layer can be characterized by introducing a local solutal Rayleigh number [37], Ra_δ, defined across the thickness δ of the boundary layer, where we have dropped the subscripts $_s$ for simplicity of notation. Introducing the dimensionless critical boundary layer thickness $\delta^* = d^*/h$, when the local Rayleigh number exceeds the critical value

$$Ra_\delta^* = Ra_s \delta^{*3}, \tag{3}$$

convection sets in in the form of downward plumes.

In the case of a biphasic system like gaseous or supercritical CO_2 over a liquid layer with free boundary conditions [42], $Ra_\delta^* = 27\pi^4/4 = 657.5$. Combining Eqs. (2) and (3), we obtain the scaling relation for the dimensionless critical time needed for the onset of the instability,

$$\tau^* = \left(\frac{Ra_s}{Ra_\delta^*}\right)^{-\frac{2}{3}}, \tag{4}$$

which is fully compatible with the experimental results shown in Fig. 4(a).

Previous experimental and theoretical works [4,5,10,11] came to the conclusion that the convective dissolution of CO_2 is slowed down by the presence of salt when the process occurs in brine, with respect to pure water. To elucidate this point, we have determined experimentally the time needed for the onset of convection in pure water and in brine obtained by adding 1 or 3 mol/kg of NaCl

TABLE I. Computation of the Rayleigh number as a function of the initial and final pressure and brine salinity. Measured values of t_c and derived d^*. The values of $x_{CO_2,0}$ and $x_{CO_2,eq}$ are the molar fractions of CO_2 in the liquid phase, respectively, at the initial and final times of the experiment.

c_{NaCl} (mol kg^{-1})	p_0 (MPa)	p_{eq} (MPa)	$x_{CO_2,0}$ (%)	$x_{CO_2,eq}$ (%)	ρ_0 (kg m^{-3})	ρ_{eq} (kg m^{-3})	$\Delta\rho$ (kg m^{-3})	Swelling factor	10^4 Ra$_s$	$t_c(s)$	d^* (mm)
0	0.10	0.33	0.0469	0.1523	994.53	995.09	0.56	1.0016	2.2	67.3	0.77
	3.08	3.59	1.2315	1.3916	1000.98	1001.93	0.96	1.0169	3.9	47.2	0.64
	0.09	0.58	0.0466	0.2620	994.53	995.67	1.14	1.0027	4.5	41.0	0.60
	0.10	1.08	0.0473	0.4775	994.53	996.81	2.28	1.0051	9.1	24.7	0.47
	0.10	2.09	0.0472	0.8812	994.53	999.00	4.46	1.0098	18.0	14.4	0.36
	0.10	3.09	0.0483	1.2343	994.54	1000.99	6.45	1.0146	26.4	12.1	0.33
	0.10	4.09	0.0481	1.5355	994.54	1002.83	8.30	1.0193	34.4	9.4	0.29
	0.10	6.08	0.0484	1.9736	994.54	1006.03	11.49	1.0287	48.9	7.7	0.26
1	4.75	6.10	1.4273	1.6432	1039.93	1041.55	1.61	1.02874	6.7	51.8	0.65
	3.85	5.10	1.2421	1.4902	1038.75	1040.37	1.62	1.0240	6.6	47.0	0.62
	2.77	4.10	0.9694	1.2965	1037.22	1039.08	1.87	1.0193	7.6	40.5	0.57
	2.08	3.10	0.7617	1.0577	1036.16	1037.69	1.53	1.0146	6.1	40.3	0.57
	1.02	2.08	0.3989	0.7647	1034.47	1036.17	1.71	1.0098	6.7	38.5	0.56
	0.09	1.07	0.0231	0.4176	1032.87	1034.55	1.68	1.0050	6.5	36.3	0.54
	3.60	6.10	1.1842	1.6439	1038.41	1041.55	3.14	1.0287	13.1	30.5	0.50
	0.09	2.08	0.0209	0.7647	1032.86	1036.17	3.31	1.0098	13.1	26.5	0.46
	3.02	6.10	1.0378	1.6432	1037.58	1041.55	3.96	1.0287	16.5	26.4	0.46
	1.90	4.10	0.7068	1.2965	1035.89	1039.08	3.19	1.0193	13.0	24.5	0.45
	0.09	3.10	0.0209	1.0577	1032.86	1037.69	4.83	1.0146	19.3	19.9	0.40
	0.09	3.83	0.0231	1.2361	1032.87	1038.72	5.85	1.0180	23.7	17.6	0.38
3	4.12	5.13	0.9950	1.1406	1104.81	1105.60	0.79	1.0242	3.3	79.0	0.72
	2.11	3.13	0.5947	0.8169	1103.10	1103.99	0.89	1.0147	3.6	67.0	0.66
	1.10	2.11	0.3294	0.5953	1102.17	1103.10	0.93	1.0100	3.7	60.7	0.63
	0.10	1.11	0.0168	0.3310	1101.19	1102.17	0.98	1.0052	3.9	46.7	0.54
	4.10	6.10	0.9920	1.2498	1104.80	1106.31	1.51	1.0287	6.4	43.5	0.59
	2.10	4.14	0.5907	0.9977	1103.09	1104.82	1.74	1.0195	7.1	46.7	0.55
	3.12	6.14	0.8159	1.2533	1103.99	1106.34	2.35	1.0289	9.9	36.0	0.48
	0.10	2.13	0.0174	0.5983	1101.19	1103.11	1.92	1.0100	7.7	35.3	0.48
	0.10	3.13	0.0173	0.8182	1101.19	1104.00	2.80	1.0148	11.4	23.8	0.39
	0.10	4.14	0.0170	0.9984	1101.19	1104.83	3.64	1.0195	15.0	17.0	0.33
	0.10	6.14	0.0168	1.2535	1101.19	1106.34	5.15	1.0289	21.7	12.5	0.28

to water. Although for the same pressure jump, the time evolution of the contrast of shadowgraph images exhibits a delayed onset of convection, once the dimensionless solutal Rayleigh number is adopted for the parametrization of the results, we find that data points for pure water and brine collapse on the same master curve expressed by Eq. (4) [Fig. 4(a)]. Therefore, the slowing down of the onset of convection in brine is only associated with the difference in the solutal Rayleigh number.

After the onset of the instability and in the presence of a stable driving concentration difference $\Delta C = C_{eq} - C_0$, the system reaches a stationary convective state where the transfer of mass occurs diffusively in the boundary layer at the critical thickness d^*, while it occurs convectively in the bulk of the sample. Mass conservation imposes that the diffusive flux $j_d = -\rho D \Delta C/d^*$ inside the boundary layer must be equal to the convective flux outside of it. Introducing the solutal Nusselt number Nu_s, also known as the Sherwood number Sh, as the ratio of the overall mass flow and the

diffusive mass flux $j_h = -\rho D \Delta C/h$ across the entire thickness of the sample yields

$$\mathrm{Nu_s} = \mathrm{Sh} = \frac{j_d}{j_h} = \frac{h}{d^*} = \frac{1}{\delta^*}. \tag{5}$$

Combining Eqs. (3)–(5) yields the scaling relation

$$\mathrm{Nu_s} = \left(\frac{\mathrm{Ra_s}}{\mathrm{Ra}_\delta^*}\right)^{\frac{1}{3}}. \tag{6}$$

The analogy with heat convection at large thermal Rayleigh numbers has been recently exploited to perform fully three-dimensional simulations of Rayleigh-Darcy convection in a porous medium [47]. These simulations showed that the confinement determined by the porous medium strongly affects the scaling relation for $\mathrm{Nu_T}$ in the large $\mathrm{Ra_T}$ regime, which becomes a proportionality relation $\mathrm{Nu_T} \propto \mathrm{Ra_T}$, in agreement with theoretical predictions [9]. Here, the T subscript corresponds to the thermal version of the dimensionless numbers, while the s subscript was related to the solutal convection. An important consequence of Eq. (5) is that the convective mass flux at steady state can be inferred from the onset time of convection t_c and thus the solutal Nusselt number $\mathrm{Nu_s} = h/d^* = h/\sqrt{\pi D t_c}$. The solutal Nusselt number is thus estimated from the measured value of t_c, rather than measured directly, like usually done in other experimental setups. Under the range of solutal Rayleigh numbers we explored, the power law exponent is (0.36 ± 0.04) [Fig. 4(b)], close to the theoretical value of $1/3$ of Eq. (6) and to the experimental exponent of 0.31 reported for turbulent heat convection over a wide range of Rayleigh numbers [26]. Going back to dimensional variables, from Eqs. (1) and (4), we obtain the remarkable result that the dimensional onset time t_c needed for the onset of convection and the convective flux j_d at the steady state do not depend on the size h of the system and represent scale-free features for the convective dissolution of CO_2:

$$t_c = \frac{1}{\pi D}\left(\frac{\rho \nu D}{g \Delta \rho} Ra_\delta^*\right)^{\frac{2}{3}}, \tag{7}$$

$$j_d = \frac{D}{\beta}\left(\frac{g}{\rho \nu D}\frac{1}{Ra_\delta^*}\right)^{\frac{1}{3}} \Delta\rho^{\frac{4}{3}}, \tag{8}$$

where $\beta = (1/\rho)(\partial\rho/\partial c)$ is the solutal expansion coefficient. The physical reason behind the absence of a dependence of t_c and j_d from the typical length scale h of the system is that the boundary layer instability occurs very rapidly, when the boundary layer thickness is still much smaller than that of the laboratory liquid sample or of the aquifer. Here, the predominant parameter that makes vary the onset time of convection and the convective flow is the density difference $\Delta\rho$ which is completely determined by the pressure difference and the salinity of the experiment. This feature is akin to thermal turbulence in a layer of fluid, where it is well-known that the heat transferred for a given temperature difference is independent of the spacing between the thermalizing plates [48].

The scaling laws presented in this paper are valid only in free media. As stated above, in the presence of a porous medium, or in Hele-Shaw configurations, the Nusselt number becomes proportional to a Rayleigh-Darcy number and thus it increases much more rapidly. Thus, the convective dissolution of CO_2 in the brine should be much more efficient than diffusion only. This approach has been used to perform fully three-dimensional simulations of heat convection at large Rayleigh-Darcy numbers and at an infinite Prandtl number, which showed that the approach proposed by Howard can be adopted successfully also in the presence of a porous medium, leading to scaling relations similar to Eqs. (3)–(6), but with different power law exponents [47]. Experiments in realistic porous media will be needed to confirm the latter theoretical predictions and understand if the boundary layer mechanism is still valid to describe the phenomenon of convective dissolution.

ACKNOWLEDGMENTS

This research was carried out under the framework of the E2S UPPA Hub Newpores and Industrial Chair CO2ES supported by the Investissements d'Avenir French program managed by ANR (No. ANR16IDEX0002). Further support from CNES is gratefully acknowledged.

APPENDIX: SOLUTAL RAYLEIGH NUMBER CALCULATIONS

The computation of the solutal Rayleigh number requires the evaluation of every thermophysical parameters occurring in Eq. (1):

1. Liquid layer thickness

Solutal Rayleigh numbers were estimated from Eq. (1) using the experimental liquid layer thickness $h = 2$ mm, corrected by the swelling factor [49] at a given pressure, and further thermophysical property data from the literature or that have been calculated. The swelling is induced by the adsorption of CO_2 in the liquid phase. The corrected liquid thickness $h' = fh$ is calculated after the correction factor f which depends on the pressure of the final equilibrium of the experiment as $f = 4.7113\times10^{-4}\ p_{eq} + 1$. The swelling factor is assumed to be independent of the salinity of brine. In the main text of the paper, we did omit to state the difference between f' and f for avoiding further notation charge. As can be noticed from Table I, the effect of the swelling on the liquid thickness is always smaller than 3%. Corresponding Ra_s data are determined at macroscopic thermodynamic equilibrium when the dissolution process is complete.

The Fick diffusion coefficient, solute self-diffusivity, and solute tracer diffusion coefficient are equal in the infinite dilution regime [50]. For that reason, diffusivity data collected from the literature are at different pressures along the vapor-liquid equilibrium. The Fick diffusion coefficient associated with pure water containing dissolved CO_2 used in the calculation of Ra_s at a temperature of 308.15 K is of 2.76×10^{-9} m^2 s^{-1}. This value was obtained from the fit to its temperature dependence [51] between 298.15 and 423.15 K using an Arrhenius-type correlation [52]. The average absolute relative deviation (AARD) and the bias between experimental and modeled diffusivities are 2.37% and −0.07%, respectively. Experimental data from other references, e.g., Refs. [53–55], were not considered. This is because the results are not consistent with the model [56] for NaCl/water mixtures, as well as because, in most cases, uncertainties were not given. The complete data set [51,53–55] collected in the literature shows a double standard deviation of 68.05% on D at $T = 308.15$ K. The Fick diffusion coefficient of CO_2 and NaCl/water mixtures were determined using a Stokes-Einstein-like model [56], wherein the hydrodynamic radius is temperature-dependent and the dynamic viscosities are taken at atmospheric pressure from Kestin *et al.* [57]. For comparison purposes, the modeled diffusivities were compared to experimental ones at $T = 298.15$ K [55,56]. The AARD and bias are 7.92% and 6.03%, where the largest deviations are associated with the old experimental data from Himmelblau [55]. At $T = 308.15$ K, we found $D = 2.59$ and 2.06×10^{-9} m^2 s^{-1} for NaCl molalities of 1 and 3 mol kg^{-1}. The same correlation provides $D = 2.79 \times10^{-9}$ m^2 s^{-1} for pure water at the same temperature, which is fully compatible with the one obtained from the Arrhenius-type correlation. These values are recalled in Table II.

TABLE II. Value of the diffusion coefficient and the dynamic viscosity for the three salinities.

c_{NaCl} (mol kg^{-1})	$10^{-9}\,D$ (m^2 s^{-1})	η_{eq} (mPa s)
0	2.79	0.719
1	2.59	0.791
3	2.06	0.982

2. Dynamic viscosity

η of brine mixtures for the three molalities of salt, i.e., (0, 1, and 3) mol kg^{-1}, at different pressures were derived from the model proposed by Kestin *et al.* [57] and are summarized in Table II. They estimated that the correlation has an overall accuracy of $\pm 0.5\%$. The influence of the amount of CO_2 dissolved in brine was neglected. This assumption is supported by the work of Fleury and Deschamps [58] who showed that a change in the molar fraction of CO_2 from 0 to 2 mol % induces a variation in η of less than 8% for NaCl molalities between 0.32 and 2.92 mol kg^{-1} and temperatures between 308.15 and 373.15 K. The larger the temperature, the smaller the variation in η. 2 mol % represents the largest amount of CO_2 dissolved in brine in our experiments [59]. Furthermore, deviations in η are smaller than the typical deviations observable between different correlations that can be found in the literature [58,60–62]. Including the variation of η as a function of the concentration of CO_2, which needs to be modeled, will give rise to larger uncertainties in our calculations of Ra_s.

Densities were calculated using PhreeqC v3.7.2a [63] embedding the Peng-Robinson equation of state [64]. Calculated densities were compared to experimental densities [65] on CO_2-saturated brine mixtures for NaCl molalities between (0 and 5) mol kg^{-1}. The AARD and bias between the experimental data and the modeled densities are 0.11% and -0.07%, respectively. The density data and density difference $\Delta\rho$ of each experiment are given in Table I.

[1] S. Manabe and R. T. Wetherald, Thermal equilibrium of the atmosphere with a given distribution of relative humidity, J. Atmos. Sci. **24**, 241 (1967).

[2] V. Masson-Delmotte, P. Zhai, A. Pirani, S. L. Connors, S. B. C. Péan, N. Caud, Y. Chen, L. Goldfarb, M. I. Gomis, M. Huang, K. Leitzell, E. Lonnoy, J. Matthews, T. K. Maycock, T. Waterfield, O. Yeleki, R. Yu, and B. Zhou (eds.), IPCC, 2021: Summary for policymakers, in Climate Change 2021: The Physical Science Basis. Contribution of Working Group I to the Sixth Assessment Report of the Intergovernmental Panel on Climate Change (Cambridge University Press, Cambridge, UK, New York, 2021).

[3] B. Gates, *How to Avoid a Climate Disaster: The Solutions We Have and the Breakthroughs We Need* (Alfred A. Knopf, New York, 2021).

[4] Y. Tang, Z. Li, R. Wang, M. Cui, X. Wang, Z. Lun, and Y. Lu, Experimental study on the density-driven carbon dioxide convective diffusion in formation water at reservoir conditions, ACS Omega **4**, 11082 (2019).

[5] C. Thomas, S. Dehaeck, and A. De Wit, Convective dissolution of CO_2 in water and salt solutions, Int. J. Greenhouse Gas Control **72**, 105 (2018).

[6] H. Emami-Meybodi, H. Hassanzadeh, C. P. Green, and J. Ennis-King, Convective dissolution of CO_2 in saline aquifers: Progress in modeling and experiments, Int. J. Greenhouse Gas Control **40**, 238 (2015).

[7] A. C. Slim, Solutal-convection regimes in a two-dimensional porous medium, J. Fluid Mech. **741**, 461 (2014).

[8] J. P. Ennis-King and L. Paterson, Role of convective mixing in the long-term storage of carbon dioxide in deep saline formations, SPE J. **10**, 349 (2005).

[9] H. E. Huppert and J. A. Neufeld, The fluid mechanics of carbon dioxide sequestration, Annu. Rev. Fluid Mech. **46**, 255 (2014).

[10] R. Khosrokhavar, G. Elsinga, R. Farajzadeh, and H. Bruining, Visualization and investigation of natural convection flow of CO_2 in aqueous and oleic systems, J. Pet. Sci. Eng. **122**, 230 (2014).

[11] V. Loodts, L. Rongy, and A. De Wit, Impact of pressure, salt concentration, and temperature on the convective dissolution of carbon dioxide in aqueous solutions, Chaos: An Interdiscip. J. Nonlinear Sci. **24**, 043120 (2014).

[12] W. A. Ambrose, S. Lakshminarasimhan, M. H. Holtz, V. Nunez-Lopez, S. D. Hovorka, and I. Duncan, Geologic factors controlling CO_2 storage capacity and permanence: Case studies based on experience with heterogeneity in oil and gas reservoirs applied to CO_2 storage, Environ. Geol. **54**, 1619 (2008).

[13] W. Amarasinghe, I. Fjelde, J.-Å. Rydland, and Y. Guo, Effects of permeability on CO_2 dissolution and convection at reservoir temperature and pressure conditions: A visualization study, Int. J. Greenhouse Gas Control **99**, 103082 (2020).

[14] W. S. Amarasinghe, I. Fjelde, and A. M. N. Flaata, Visual investigation of CO_2 dissolution and convection in heterogeneous porous media at reservoir temperature and pressure conditions, Greenhouse Gases: Sci. Technol. **11**, 342 (2021).

[15] S. Mojtaba, R. Behzad, N. M. Rasoul, and R. Mohammad, Experimental study of density-driven convection effects on CO_2 dissolution rate in formation water for geological storage, J. Nat. Gas Sci. Eng. **21**, 600 (2014).

[16] H. Vosper, K. Kirk, C. Rochelle, D. Noy, and A. Chadwick, Does numerical modelling of the onset of dissolution-convection reliably reproduce this key stabilization process in CO_2 storage? Energy Procedia **63**, 5341 (2014).

[17] R. Outeda, C. E. Hasi, A. D'Onofrio, and A. Zalts, Experimental study of linear and nonlinear regimes of density-driven instabilities induced by CO_2 dissolution in water, Chaos **24**, 013135 (2014).

[18] T. F. Faisal, S. Chevalier, Y. Bernabe, R. Juanes, and M. Sassi, Quantitative and qualitative study of density driven CO_2 mass transfer in a vertical Hele-Shaw cell, Int. J. Heat Mass Transf. **81**, 901 (2015).

[19] A. Vreme, F. Nadal, B. Pouligny, P. Jeandet, G. Liger-Belair, and P. Meunier, Gravitational instability due to the dissolution of carbon dioxide in a Hele-Shaw cell, Phys. Rev. Fluids **1**, 064301 (2016).

[20] G. Lu, Y. Liu, L. Jiang, T. Ying, Y. Song, and B. Wu, Study of density driven convection in a Hele-Shaw cell with application to the carbon sequestration in aquifers, Energy Procedia **114**, 4303 (2017).

[21] A. Taheri, O. Torsæter, E. Lindeberg, N. J. Hadia, and D. Wessel-Berg, Qualitative and quantitative experimental study of convective mixing process during storage of CO_2 in heterogeneous saline aquifers, Int. J. Greenhouse Gas Control **71**, 212 (2018).

[22] Y. Teng, P. Wang, L. Jiang, Y. Liu, and Y. Wei, New spectrophotometric method for quantitative characterization of density-driven convective instability, Polymers **13**, 661 (2021).

[23] M. De Paoli, M. Alipour, and A. Soldati, How non-Darcy effects influence scaling laws in Hele-Shaw convection experiments, J. Fluid Mech. **892**, A41 (2020).

[24] E. Lindeberg and D. Wessel-Berg, Vertical convection in an aquifer column under a gas cap of CO_2, Energy Convers. Manage. **38**, S229 (1997).

[25] E. D. Siggia, High Rayleigh number convection, Annu. Rev. Fluid Mech. **26**, 137 (1994).

[26] J. J. Niemela, L. Skrbek, K. R. Sreenivasan, and R. J. Donnelly, Turbulent convection at very high Rayleigh numbers, Nature (London) **404**, 837 (2000).

[27] S. Grossmann and D. Lohse, Thermal Convection for Large Prandtl Numbers, Phys. Rev. Lett. **86**, 3316 (2001).

[28] A. S. Fleischer and R. J. Goldstein, High-Rayleigh-number convection of pressurized gases in a horizontal enclosure, J. Fluid Mech. **469**, 1 (2002).

[29] F. Croccolo and D. Brogioli, Quantitative Fourier analysis of schlieren masks: The transition from shadowgraph to schlieren, Appl. Opt. **50**, 3419 (2011).

[30] W. Wu, J. H. Jander, M. H. Rausch, A. P. Fröba, and C. Giraudet, Simultaneous determination of multiple transport properties over a wide range of temperatures and pressures from the analysis of non-equilibrium fluctuations by the shadowgraph method, J. Chem. Phys. **153**, 144201 (2020).

[31] F. Croccolo, H. Bataller, and F. Scheffold, A light scattering study of non equilibrium fluctuations in liquid mixtures to measure the Soret and mass diffusion coefficient, J. Chem. Phys. **137**, 234202 (2012).

[32] F. Croccolo, F. Scheffold, and A. Vailati, Effect of a Marginal Inclination on Pattern Formation in a Binary Liquid Mixture Under Thermal Stress, Phys. Rev. Lett. **111**, 014502 (2013).

[33] C. Giraudet, H. Bataller, Y. Sun, A. Donev, J. M. Ortiz de Zárate, and F. Croccolo, Confinement effect on the dynamics of non-equilibrium concentration fluctuations far from the onset of convection, Eur. Phys. J. E **39**, 120 (2016).

[34] N. Spycher, K. Pruess, and J. Ennis-King, CO_2-H_2O mixtures in the geological sequestration of CO_2. I. Assessment and calculation of mutual solubilities from 12 to 100°C and up to 600 bar, Geochim. Cosmochim. Acta **67**, 3015 (2003).

[35] See Supplemental Material at http://link.aps.org/supplemental/10.1103/PhysRevFluids.8.023503 for a movie showing differences of Shadowgraph images upon pressure increase of CO_2 from 0.1 to 2.0 MPa as well as their contrast as a function of time.
[36] M. R. Soltanian, M. A. Amooie, Z. Dai, D. Cole, and J. Moortgat, Critical dynamics of gravito-convective mixing in geological carbon sequestration, Sci. Rep. **6**, 35921 (2016).
[37] H. Görtler, *Applied Mechanics: Proceedings of the Eleventh International Congress of Applied Mechanics Munich (Germany) 1964* (Springer, Berlin, 1966).
[38] S. Mazzoni, R. Cerbino, D. Brogioli, A. Vailati, and M. Giglio, Transient oscillations in Soret-driven convection in a colloidal suspension, Euro. Phys. J. E **15**, 305 (2004).
[39] R. Cerbino, S. Mazzoni, A. Vailati, and M. Giglio, Scaling Behavior for the Onset of Convection in a Colloidal Suspension, Phys. Rev. Lett. **94**, 064501 (2005).
[40] F. Giavazzi and A. Vailati, Scaling of the spatial power spectrum of excitations at the onset of solutal convection in a nanofluid far from equilibrium, Phys. Rev. E **80**, 015303(R) (2009).
[41] F. Winkel, S. Messlinger, W. Schöpf, I. Rehberg, M. Siebenbürger, and M. Ballauff, Thermal convection in a thermosensitive colloidal suspension, New J. Phys. **12**, 053003 (2010).
[42] S. Messlinger, W. Schöpf, and I. Rehberg, Transient diffusive boundary layers at high Rayleigh numbers in simple and double diffusive fluids: Latency time scaling for the convection onset, Int. J. Heat Mass Transf. **62**, 336 (2013).
[43] J. Philippi, M. Berhanu, J. Derr, and S. Courrech du Pont, Solutal convection induced by dissolution, Phys. Rev. Fluids **4**, 103801 (2019).
[44] T. S. Sullivan, Y. Liu, and R. E. Ecke, Turbulent solutal convection and surface patterning in solid dissolution, Phys. Rev. E **54**, 486 (1996).
[45] J. Crank, *The Mathematics of Diffusion* (Oxford University Press, Oxford, UK, 1975).
[46] F. Croccolo, J. M. Ortiz de Zárate, and J. V. Sengers, Non-local fluctuation phenomena in liquids, Eur. Phys. J. E **39**, 125 (2016).
[47] S. Pirozzoli, M. De Paoli, F. Zonta, and A. Soldati, Towards the ultimate regime in Rayleigh–Darcy convection, J. Fluid Mech. **911**, R4 (2021).
[48] J. W. Elder, The unstable thermal interface, J. Fluid Mech. **32**, 69 (1968).
[49] X. Li, Y. Song, B. Wu, Y. Liu, and L. Jiang, Determination of swelling effect in CO_2-brine systems using microfocus X-ray CT, Energy Procedia **142**, 3344 (2017).
[50] W. Wu, T. Klein, M. Kerscher, M. H. Rausch, T. M. Koller, C. Giraudet, and A. P. Fröba, Diffusivities in 1-alcohols containing dissolved H_2, He, N_2, CO, or CO_2 close to infinite dilution, J. Phys. Chem. B **123**, 8777 (2019).
[51] S. P. Cadogan, G. C. Maitland, and J. P. M. Trusler, Diffusion coefficients of CO_2 and N_2 in water at temperatures between 298.15 K and 423.15 K at pressures up to 45 MPa, J. Chem. Eng. Data **59**, 519 (2014).
[52] C. Giraudet, T. Klein, G. Zhao, M. H. Rausch, T. M. Koller, and A. P. Fröba, Thermal, mutual, and self-diffusivities of binary liquid mixtures consisting of gases dissolved in *n*-alkanes at infinite dilution, J. Phys. Chem. B **122**, 3163 (2018).
[53] M. J. Frank, J. A. Kuipers, and W. P. van Swaaij, Diffusion coefficients and viscosities of $CO_2 + H_2O$, $CO_2 + CH_3OH$, $NH_3 + H_2O$, and $NH_3 + CH_3OH$ liquid mixtures, J. Chem. Eng. Data **41**, 297 (1996).
[54] A. A. Unver and D. M. Himmelblau, Diffusion coefficients of CO_2, C_2H_4, C_3H_6 and C_4H_8 in water from 6° to 65°C, J. Chem. Eng. Data **9**, 428 (1964).
[55] D. M. Himmelblau, Diffusion of dissolved gases in liquids, Chem. Rev. **64**, 527 (1964).
[56] S. P. Cadogan, J. P. Hallett, G. C. Maitland, and J. P. M. Trusler, Diffusion coefficients of carbon dioxide in brines measured using ^{13}C pulsed-field gradient nuclear magnetic resonance, J. Chem. Eng. Data **60**, 181 (2015).
[57] J. Kestin, E. H. Khalifa, and R. J. Correia, Tables of the dynamic and kinematic viscosity of aqueous NaCl solutions in the temperature range 20-150°C and the pressure range 0.1-35 MPa, J. Phys. Chem. Ref. Data **10**, 71 (1981).
[58] M. Fleury and H. Deschamps, Electrical conductivity and viscosity of aqueous NaCl solutions with dissolved CO_2, J. Chem. Eng. Data **53**, 2505 (2008).

[59] L. W. Diamond and N. N. Akinfiev, Solubility of CO_2 in water from -1.5 to 100°C and from 0.1 to 100 MPa: Evaluation of literature data and thermodynamic modelling, Fluid Phase Equilib. **208**, 265 (2003).

[60] A. Kumagai and C. Yokoyama, Viscosities of aqueous NaCl solutions containing CO_2 at high pressures, J. Chem. Eng. Data **44**, 227 (1999).

[61] S. Bando, F. Takemura, M. Nishio, E. Hihara, and M. Akai, Viscosity of aqueous NaCl solutions with dissolved CO_2 at (30 to 60) °C and (10 to 20) MPa, J. Chem. Eng. Data **49**, 1328 (2004).

[62] A. W. Islam and E. S. Carlson, Viscosity models and effects of dissolved CO_2, Energy Fuels **26**, 5330 (2012).

[63] D. L. Parkhurst and C. A. J. Appelo, Description of input and examples for PHREEQC version 3–A computer program for speciation, batch-reaction, one-dimensional transport, and inverse geochemical calculations, *Techniques and Methods, 6* (U.S. Geological Survey, 2013), Chap. A43, p. 497, https://pubs.usgs.gov/tm/06/a43/.

[64] D.-Y. Peng and D. B. Robinson, A new two-constant equation of state, Ind. Eng. Chem. Fund. **15**, 59 (1976).

[65] W. Yan, S. Huang, and E. H. Stenby, Measurement and modeling of CO_2 solubility in NaCl brine and CO_2-saturated NaCl brine density, Int. J. Greenhouse Gas Control **5**, 1460 (2011).